








RESEARCH ARTICLE | JULY 23 2024

## Evolution of downburst-like flows produced by an active-controlled multi-blade facility

Yangjin Yuan (袁养金) ; Bowen Yan (闫渤文)  ; Xuhong Zhou (周绪红); Xiao Li (李潇) ; You Dong (董优) ; Qingshan Yang (杨庆山) ; Qingkuan Liu (刘庆宽) 



*Physics of Fluids* 36, 077152 (2024)

<https://doi.org/10.1063/5.0220379>



View  
Online



Export  
Citation

### Articles You May Be Interested In

Temporal variability wind characterization analysis and model construction of moving downbursts

*Physics of Fluids* (January 2025)

Energy-based wind field reconstruction and extrema estimation for downburst events

*Physics of Fluids* (November 2025)

Experimental investigation of downburst-induced wind loads on rectangular high-rise buildings: Influence of geometric features

*Physics of Fluids* (August 2025)



Physics of Fluids

Special Topics Open  
for Submissions

[Learn More](#)

# Evolution of downburst-like flows produced by an active-controlled multi-blade facility

Cite as: Phys. Fluids **36**, 077152 (2024); doi: [10.1063/5.0220379](https://doi.org/10.1063/5.0220379)

Submitted: 24 May 2024 · Accepted: 3 July 2024 ·

Published Online: 23 July 2024



View Online



Export Citation



CrossMark

Yangjin Yuan (袁养金),<sup>1</sup>  Bowen Yan (闫渤文),<sup>1,a)</sup>  Xuhong Zhou (周绪红),<sup>1</sup> Xiao Li (李潇),<sup>1</sup>  You Dong (董优),<sup>2</sup>  Qingshan Yang (杨庆山),<sup>1</sup>  and Qingkuan Liu (刘庆宽)<sup>3</sup> 

## AFFILIATIONS

<sup>1</sup>Key Laboratory of New Technology for Construction of Cities in Mountain Area (Ministry of Education), School of Civil Engineering, Chongqing University, Chongqing 400045, China

<sup>2</sup>Department of Civil and Environmental Engineering, The Hong Kong Polytechnic University, Kowloon, Hung Hom, Hong Kong, China

<sup>3</sup>State Key Laboratory of Mechanical Behavior and System Safety of Traffic Engineering Structures, Shijiazhuang Tiedao University, Shijiazhuang 050043, China

<sup>a)</sup>Author to whom correspondence should be addressed: [bowenyancq@cqu.edu.cn](mailto:bowenyancq@cqu.edu.cn)

## ABSTRACT

The intricate dynamics of vortex structures within the downburst outflow region present significant challenges in studying flow evolutionary features, which are crucial for understanding the effect of such flow on various structures. This study aims to reveal the evolutionary features of downburst-like winds produced by an active-controlled multi-blade (AMBS) facility, using the particle image velocimetry tests and the large-eddy simulation (LES) studies. The numerical simulation indicates that the wind velocity profiles, nonstationary wind velocity time history, and the transient flow patterns of the downward flow impinging on the ground can be well simulated by the LES method. For stationary winds, a series of columnar vortices are produced, and the vortices tend to be more organized as the maximum velocity appears at a lower height. The proper orthogonal decomposition analysis manifests that the primary vortex region is affected by multiple modes of the fluctuating wind field. In addition, the primary vortex structures of the AMBS-generated flow present apparent evolutionary features. During the downward flow impinging on the ground, the nose-shaped wind velocity profile gradually forms at the turntable center and is well developed when the maximum velocity is reached. This observation is in accordance with the findings in available full-scale measurement campaigns.

Published under an exclusive license by AIP Publishing. <https://doi.org/10.1063/5.0220379>

## I. INTRODUCTION

Thunderstorm downbursts have captured growing attention in the wind engineering community due to their negative effect on structures. The outflow generated after downward flow impinging the ground has been regarded as the primary reason for the generation of violent horizontal winds, which deals severe damage to infrastructure structures (e.g., Kwon and Kareem, 2009; Solari, 2016; Le and Caracoglia, 2017; Kwon and Kareem, 2019; and Zhang *et al.*, 2022). The downburst outflow typically exhibits intense horizontal velocities, a “nose-shaped” profile, and a nonstationary temporal variation. Much effort has been made to acquire a deep understanding of the characteristics of downburst outflows based on full-scale measurements (e.g., Hjelmfelt, 1988; Solari *et al.*, 2020; Zhang *et al.*, 2019; and Liu *et al.*, 2023), experimental methods (e.g., Fang *et al.*, 2023; Junayed *et al.*, 2019), numerical computational fluid dynamics (CFD) methods (e.g., Mason *et al.*, 2009; Yan *et al.*, 2022), and analytical methods (e.g.,

Abd-Elaal *et al.*, 2013; Li *et al.*, 2012). In particular, the ERC AdG THUNDERR Project, a milestone research project in wind engineering, conducted by Prof. G. Solari and his research group at the University of Genoa has systematically investigated thunderstorms and their effects on structures based on a series of field measurements, experiments, and numerical simulation studies (Solari *et al.*, 2020). Full-scale downburst wind velocity data acquisition campaigns can provide essential benchmarks for experimental and numerical studies, while these wind field records are difficult to acquire due to the high randomness of downburst occurrence in terms of time and place. As a result, many researchers attempted to generate the downburst outflows by different experimental and numerical methods.

The impinging jet (IJ) method is widely used to replicate the downburst. This method utilizes a momentum-forcing source (fan or other air-driving equipment) to direct flow to impinge onto the ground to mimic the downdraft process of downburst winds in nature, while

the buoyancy effects are neglected. The IJ method is highly capable of recreating the outflow mechanisms, such as the “nose shape” wind profile and primary vortex structures, which is supported by a large body of studies using steady IJ methods (e.g., Wood *et al.*, 2001; Kim and Hangan, 2007; Sengupta and Sarkar, 2008; and Zhang *et al.*, 2014) or their “pulsed” versions (e.g., Mason *et al.*, 2005; Jesson *et al.*, 2015a; 2015b; and Romanic *et al.*, 2019). Moreover, the movable nozzle of IJ simulators was also developed to investigate the wind fields during the moving downburst (e.g., Asano *et al.*, 2019; Wu *et al.*, 2021; and Fang *et al.*, 2023). However, the generated downburst needs to match the length scale of the investigated structures, which requires a considerably large IJ simulator to generate the downburst flows that are sufficiently large to meet the requirement of the Reynolds number effect on a scaled structure model. To this end, a much larger test chamber was established at the WindEEE Dome, which was capable of replicating the downburst winds in a large scale. Thus, it allowed the tests carried out on the models with relatively larger length scale (Hangan *et al.*, 2017a; 2017b; and 2019). Nevertheless, larger scale IJ simulators mean increased input of experimental cost. In reality, the characteristic of downburst outflow is the full process of the downburst in the experiment because the effect of downburst outflow on structures is much concerned due to its large horizontal wind velocity and nonstationary properties. Therefore, some researchers tried to design additional devices to mimic downburst-like outflows in conventional boundary layer wind tunnels instead of the entire downburst.

In the boundary layer wind tunnel, additional experimental tools are employed to redirect the horizontal flow toward the ground to produce nonstationary outflows (Butler and Kareem, 2007; 2009; Le and Caracoglia, 2019; Aboutabikh *et al.*, 2019; and Mejia *et al.*, 2022). These techniques are capable of mimicking two-dimensional outflows, which can be regarded as a vertical slice of the radial flows produced by IJ simulators. In the implementation of Butler and Kareem (2007, 2009), a large flat plate with a large inclined angle was added upstream to redirect the horizontal flows to imping on the ground. The nose-shaped wind profiles can be generated in their tests, while the adjustment of the wind profile and simulation of nonstationary wind velocity are difficult. Recently, a multi-blade flow device (Le and Caracoglia, 2019; Aboutabikh *et al.*, 2019) has been reported in the available literature, which has an improved controllability of the generated outflows. Le and Caracoglia (2019) replicated a nonstationary wind similar to the full-scale Andrews AFB thunderstorm wind velocity records (Fujita, 1985). In addition, the Unsteady Reynolds Averaging Navier–Stokes (URANS) method was used to investigate the produced wind flows, while only the speed-up region can be observed in the simulated wind field, and the primary vortex was not observed. Aboutabikh *et al.* (2019) designed and calibrated a blade system that was capable of generating downburst outflows. Moreover, the wind flow features produced by static and rotating blade configurations were investigated using the large-eddy simulation (LES) method. Furthermore, Yuan *et al.* (2024) improved the blade system and designed an Active-controlled multi-blade facility, of which each blade can be controlled individually. The mean wind profiles and noteworthy nonstationary features obtained in the field measurements can be appropriately replicated by this facility. It is noted that their studies mainly focused on the nonstationary wind velocity records at limited specific locations, while the flow evolutionary features of the multi-blade generated winds were not comprehensively investigated. In view of this, the present

study aims to fulfill this problem to promote the multi-blade generated flows, which can be employed to investigate the effects of downburst outflow on structures.

The investigation of wind field evolution is important to reveal the underlying nonstationary mechanisms behind downburst winds and to further the understanding of the wind effects on structures subjected to downburst winds. Canepa *et al.* (2020) investigated the evolution features of the vertical profile in the outflow region based on full-scale downburst records, concluding that typical nose-shaped wind profiles appear during the velocity ramp-up and peak stages. Junayed *et al.* (2019) analyzed the variation of mean velocity and turbulent intensity profiles, concerning the height-to-diameter ratios based on synchronous point velocity measurements in the WindEEE Dome. Moreover, the vortex dynamics were investigated by conducting the particle image velocimetry (PIV) measurements on a radial 2D planar. Compared with the experimental methods, the numerical simulation method might have its unique advantage in investigating the evolution features of flow structures. A large body of available literature reported the evolutionary flow structures of downbursts simulated by the IJ method based on numerical simulations (e.g., Mason *et al.*, 2009; Aboshosha *et al.*, 2015; Ibrahim *et al.*, 2020; and Zuzul *et al.*, 2023). In these studies, the evolutionary characteristics of the wind flow at the outflow region were well replicated in terms of different numerical methods, providing useful information regarding the evolutionary characteristics of wind flows during the occurrence of downburst winds.

The present paper mainly addressed the evolution of downburst-like outflow generated by an novel active-controlled multi-blade system in a boundary layer wind tunnel. The design and calibration of the active-controlled multi-blade system (AMBS) was reported by Yuan *et al.* (2024), while the evolution of AMBS-generated downburst-like outflow was not systematically studied. In our previous work, a group of downburst-like wind profiles was produced by adjusting the configuration of blade rotation, and these wind profiles matched well with the target profiles obtained from full-scale measurements of actual downbursts. In addition, several nonstationary wind fields with different peak velocity durations were also produced and analyzed systematically. The present study aims to investigate the underlying mechanisms of the wind flows produced by the AMBS facility under static and rotating blade configurations based on the LES studies. The PIV measurements were conducted to capture the vortex dynamics at the turntable range along the streamwise direction during the rotation of blades. The LES method was validated by the results of point velocity measurements and PIV experiments. Furthermore, the flow evolutionary features of the winds produced by static and rotating blade configuration were investigated by utilizing the superiority of numerical simulation in extracting full-field information. The proper orthogonal decomposition (POD) method was employed to analyze the deterministic vortex structures in the wind flows generated by static blade configuration.

This paper is organized into the following sections: Sec. II describes the details of the wind tunnel experimental and numerical setup. Section III presents the validation of numerical results, including the wind profiles along the streamwise direction, nonstationary wind velocity at the reference height, and the wind velocity distribution patterns during the blade rotation. Section IV discusses the underlying evolutionary mechanisms of the wind fields produced by static and rotating blade configurations. Finally, the primary conclusions are summarized in Sec. V.

## II. EXPERIMENTAL AND NUMERICAL SETUP

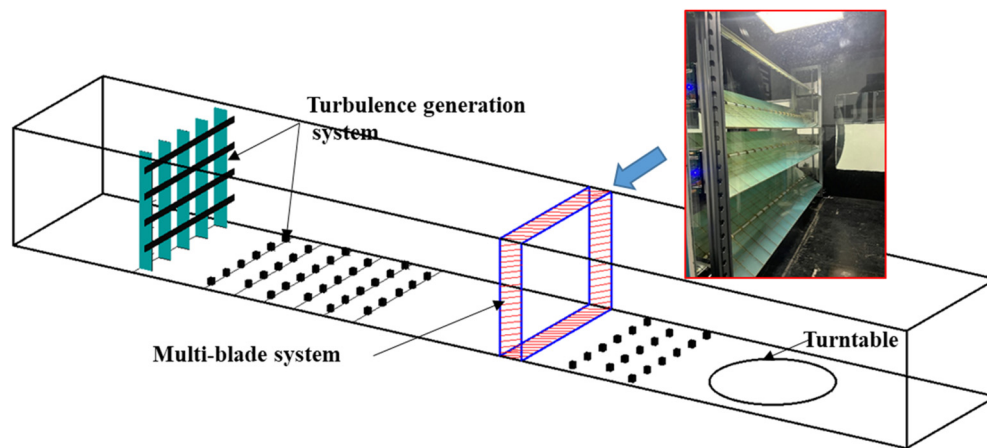
In this section, the experimental details and CFD modeling method in the present study are introduced. First, details about the wind velocity measurements using the AMBS are presented in Sec. II A, followed by a detailed description of the arrangements for the PIV tests in Sec. II B. Additionally, the setup of CFD simulation in the present study is described in Sec. II C.

### A. Introduction of wind velocity measurements

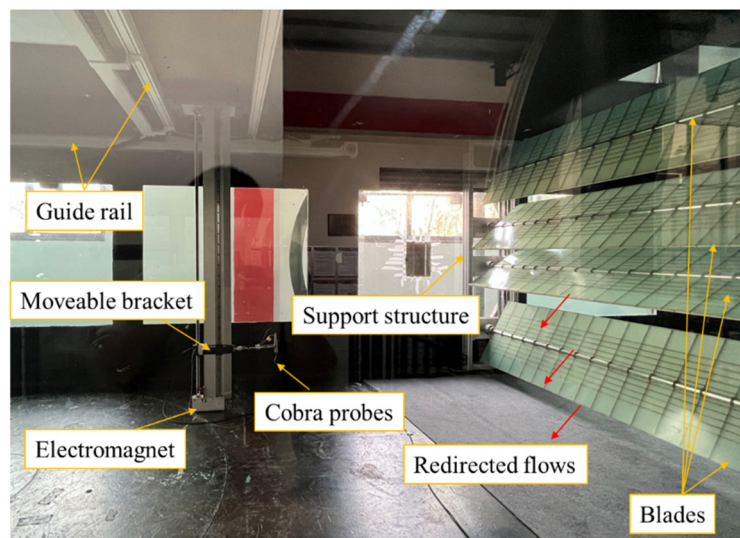
The wind tunnel tests are conducted in the atmospheric boundary layer (ABL) wind tunnel at Chongqing University (CQU), an open-circuit type with a cross section dimension of 2.4 m (breadth)  $\times$  1.8 m

(height). The schematic diagrams of the entire wind tunnel and its test section are shown in Fig. 1(a). The maximum wind velocity of 30 m/s can be reached in the test section.

The AMBS is installed at the position upstream of the turntable, and the horizontal distance between the AMBS installation location and the turntable center is 3 m [Fig. 2(a)]. The grid installed at the inlet can be utilized to enhance the turbulence of the approaching flow, and the roughness elements are used to adjust the flow near the ground. The AMBS is only briefly introduced herein, and readers are referred to our previous work (Yuan *et al.*, 2024) for more details of the AMBS design. To measure the evolutionary features of the AMBS-generated downburst-like outflows, the measurement locations are arranged as shown in Fig. 2. The measurement area is consisted of 35 horizontal



(a) Diagram of the wind tunnel and AMBS



(b) Arrangement in wind tunnel tests

FIG. 1. Wind tunnel layout of the AMBS device. (a) Diagram of the wind tunnel and AMBS. (b) Arrangement in wind tunnel tests.

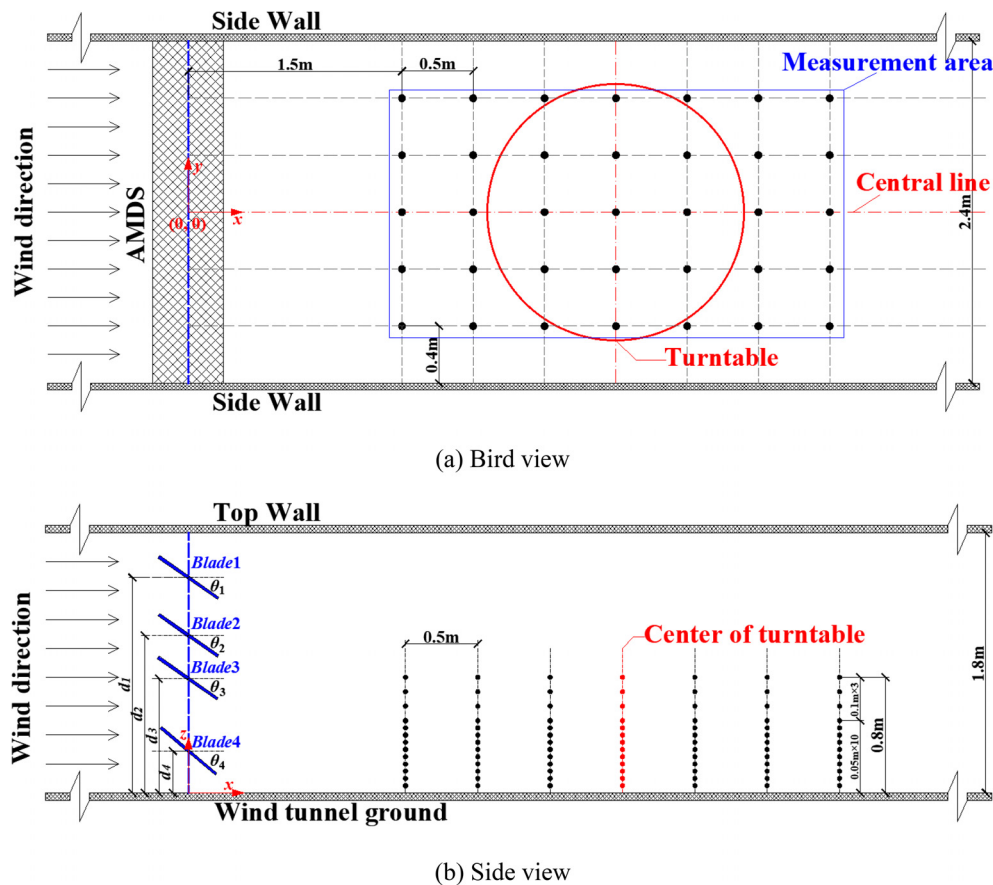


FIG. 2. The diagram of the measurement locations. (a) Bird view. (b) Side view.

locations with streamwise and spanwise intervals of 0.5 and 0.4 m, respectively [Fig. 2(a)]. Thirteen measurement positions ( $z = 0.05, 0.1, 0.15, 0.2, 0.25, 0.3, 0.35, 0.4, 0.45, 0.5, 0.6, 0.7, \text{ and } 0.8 \text{ m}$ ) are set in the vertical direction at each horizontal position [Fig. 2(b)]. For the ease of description, the location of each blade and its associated rotation configuration are also illustrated in Fig. 2(b). In the present study, the values of  $d_1$ – $d_4$  are set to be 1.5, 1.1, 0.8, and 0.3 m, respectively. The rotation configurations of the blades can be independently adjusted to simulate various downburst-like outflows.

## B. PIV setup

Aside from the point velocity measurements performed utilizing Cobra probes, the AMBS-generated downburst outflow in the central vertical plane ( $y = 0 \text{ m}$ ) is also measured employing the PIV test. As shown in Fig. 3(a), two high-speed cameras are used in the wind tunnel to capture the produced outflows in a region of 0.8 m (width) by 0.8 m (height). The resolution of the cameras is set to  $1024 \times 1024$  pixels, and the sampling rate of 2000 Hz is adopted in the present test. The minimum exposure time of each camera is  $1.05 \mu\text{s}$ . The shooting coverage of the two cameras is calibrated carefully before the PIV tests. The tracer particles with an average diameter of  $1\text{--}5 \mu\text{m}$  are released at the inlet of the wind tunnel. The released tracer particles could be

reconstructed to be uniformly distributed after passing through the screens of the wind tunnel. In addition, a high repetition frequency pulsed laser is placed at the outlet of the wind tunnel. To ensure the quality of each snapshot, the parameter of the laser device is properly adjusted before the PIV experiments. The wavelength is set to be 527 nm with a pulse width of  $\sim 200 \text{ ns}$ . The repetition rate of the laser is 0.2 k–10 kHz, with the energy of  $30 \text{ mJ} \times 2 \text{ path} @ 1 \text{ kHz}$  and energy stability (RMS) below 1%. As shown in Fig. 3(b), partial regions of the blades are painted black to reduce the exposure of the snapshot. Furthermore, the velocity at the reference height is measured by Cobra probes synchronously to make sure the produced wind field matches the velocity field measured in Sec. II A.

## C. CFD modeling

Although the PIV test in the present study has presented the flow structures in the streamwise direction in a two-dimensional plane, the three-dimensional structures of vortices cannot be well demonstrated. In addition, only a limited region of the AMBS-generated flow near the ground was captured by the PIV test, while the full process of the flow development in the entire wind tunnel region could not be observed. To provide more comprehensive information regarding the flow generated by the AMBS, large-eddy simulation is conducted to

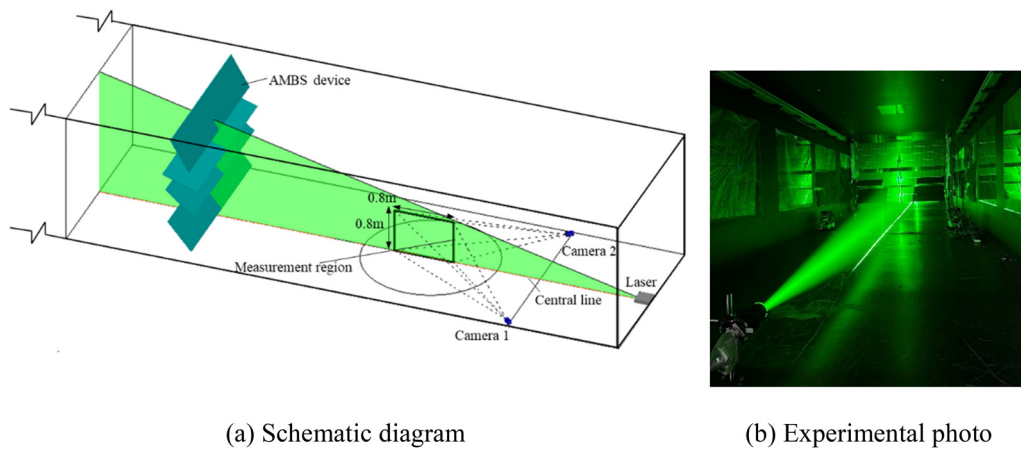


FIG. 3. Experimental arrangements for PIV measurements. (a) Schematic diagram. (b) Experimental photo.

shed insights into the spatial distribution of wind velocity during the generation process of the nonstationary winds. The wind tunnel and the AMBS facility are modeled in the numerical simulation according to their geometrical dimension. In this section, the computational domain and employed boundary conditions are first introduced. Then, the mesh schemes for the static blade and dynamic rotating blade configurations are presented in the next subsection as well as the solution strategies adopted in the present study. The data sampling details are described in the last subsection.

### 1. Computational domain and boundary conditions

Figure 4 illustrates the diagram of the computational domain. The geometry of the AMBS blades is established according to the experimental device installed in the wind tunnel. The distances between any two blades and the rotating configurations of the blades are set to be the same as the conditions adopted in the wind tunnel tests (Yuan *et al.*, 2024). The cross section of the computational domain is the same as that of the wind tunnel, while the streamwise dimension is shortened to improve the computational efficiency. The AMBS model is placed at  $x = 0$  m, and the inlet and outlet boundaries are set at  $x = -2$  m and  $x = 6$  m, respectively. To replicate the flows produced in the wind tunnel test, the uniform velocity of 7 m/s is

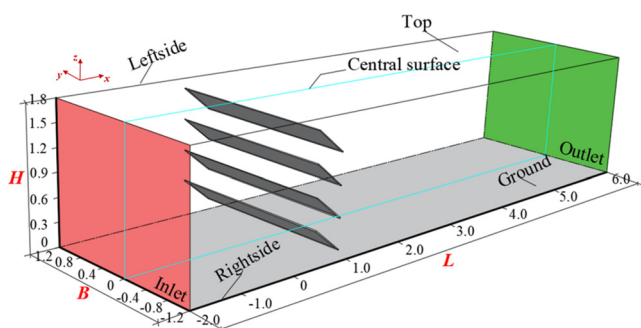


FIG. 4. Computational domain diagram.

imposed on the Inlet surface of the computational domain. The outlet surface is set as the outflow boundary condition. The Leftside, Rightside, and Top surfaces are defined as the symmetry boundary conditions.

### 2. Computational mesh and solution strategies

To realize the simulation case of static blade and rotating blade configurations, two types of computational mesh are utilized in the present study. Figure 5(a) shows the first kind of mesh, where each blade maintains its predefined rotation angle throughout the whole simulation. To resolve the flows near the blade edge, the nearby mesh is further refined. Moreover, the mesh behind the AMBS is also refined to resolve the flow of interest. As illustrated in Fig. 5(b), the overset mesh is employed to serve as the dynamic mesh strategy. Each blade is set as an independent region, named region 1, region 2, region 3, and region 4, which can rotate independently around its centroid. The background mesh (apart from regions 1 to 4) is defined as region 0. The numerical data between each blade region and background mesh is transferred based on interpolation during the simulation. The *multiSolidBodyMotionSolver* is used to deal with the dynamic mesh. The rotating angle time history of each blade is controlled by the *tabulated6DofMotion* entry, where the translational and rotational motion of a body can be predefined in a tabulated file. A code to generate the tabulated file, defining arbitrary rotating blade configuration, is developed based on OpenFoam.

The mesh independence studies for both static and rotating blade configurations are conducted with three different levels of mesh refinement (Mesh1, Mesh2, and Mesh3) at the region of interest. The mean wind velocity profiles at  $(x, y) = (3.0 \text{ m}, 0 \text{ m})$  are used for comparison. The results of the grid independence examination are presented in Fig. 6. Figure 6(a) presents the mean wind velocity profile and Fig. 6(b) plots the transient wind velocity profile after the finishment of blade rotation. In addition, the relative errors [Eq. (1)] among different mesh schemes are also presented in Fig. 6(c). It can be found the relative error between Mesh 2 and Mesh 1 is 2.1% and 3.8% for static and rotating blade configurations, respectively. In contrast, the variation of the wind velocity profiles is limited with the mesh being further

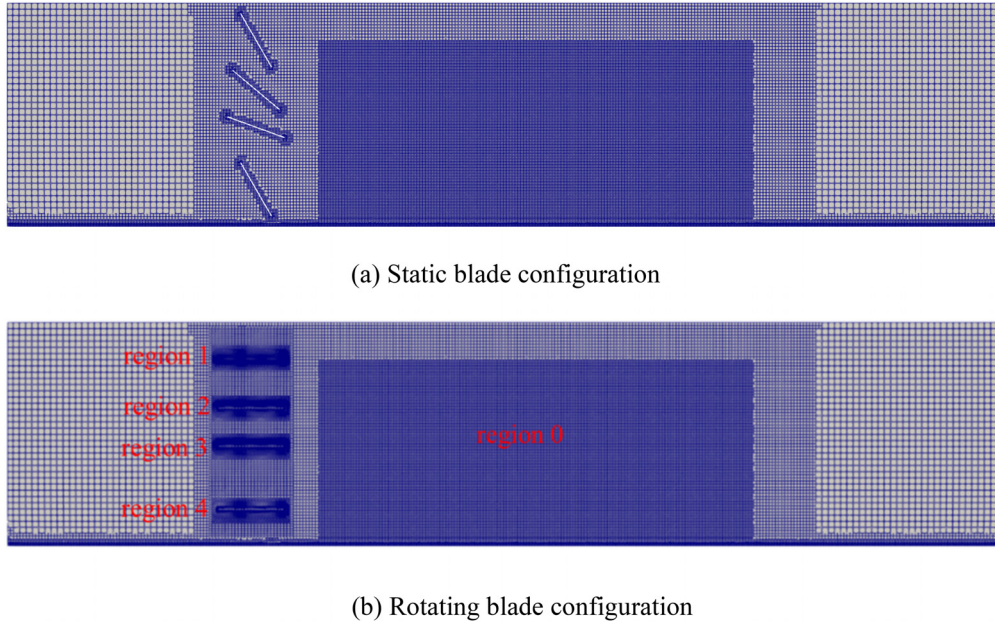


FIG. 5. Computational mesh. (a) Static blade configuration. (b) Rotating blade configuration.

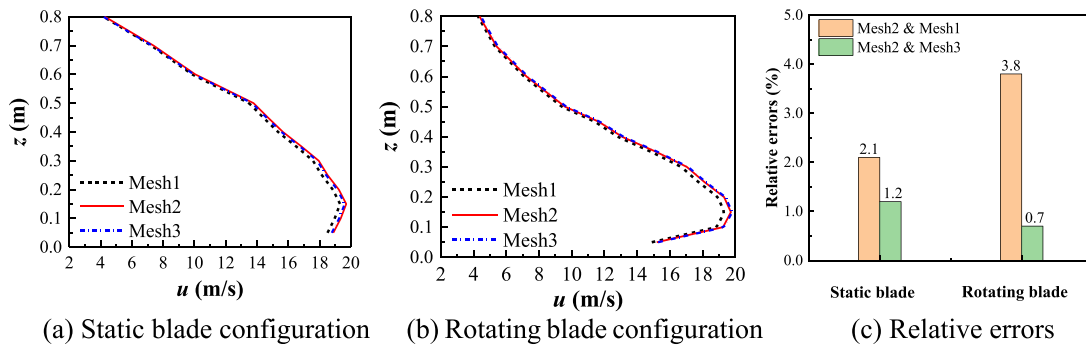


FIG. 6. The examination of mesh independence. (a) Static blade configuration. (b) Rotating blade configuration. (c) Relative errors.

refined. Therefore, the Mesh2 of the static and rotating blade cases depicted in Fig. 5 is adopted for the sake of balance between computational accuracy and efficiency. The smallest cell in the Mesh2 is approximately  $6.3 \times 10^{-4}$  m ( $y+ < 5$ ), mainly located at the near-wall region of the blades and the ground. The total cell count for each case is approximately  $9.0 \times 10^6$ ,

$$\varepsilon_u = \frac{\int_0^h |u_{tar}(z) - u(z)| dz}{\int_0^h u_{tar}(z) dz}, \quad (1)$$

where  $u_{tar}$  is the target mean streamwise velocity and turbulence intensity components.  $\varepsilon_u$  is the relative error of  $u$  profiles. The integral interval  $(0, h)$  in the above definition is determined by the considered height range of the wind profiles.

The numerical simulations are performed with the open-source software OpenFoam-v2206 based on the finite volume method. The kinematic viscosity coefficient is set to  $1.5 \times 10^{-5}$  m<sup>2</sup>/s to mimic the air properties in the wind tunnel test. The flow field is calculated using the LES model based on the filtered Navier–Stokes equations for incompressible flow. The standard Smagorinsky–Lilly model ( $C_s = 0.1$ ) is employed to model the subgrid-scale turbulence. The pressure-implicit with the splitting of operators (PISOs) algorithm is employed to resolve the velocity-pressure coupled equations of the transient flow. The time-derivative term is discretized with the Euler scheme, and the linear-upwind scheme is adopted to discretize the convective term of the momentum equation. For the diffusion term, the second-order central difference scheme is applied. Additionally, the pressure gradient terms are resolved using the scheme of Gaussian integration with linear interpolation. The time integrations are processed with a fully implicit scheme. All the simulations are

performed on the workstation in parallel (Intel Xeon Platinum 8269CY, 52 cores, 256G memory).

### 3. Data sampling in LES

The velocity sampling is divided into two groups. For the first group, the velocity is synchronously sampled by probes according to the arrangements of the measurement positions adopted in wind tunnel tests. For the second group, the wind velocity field at the cutting planes of  $y = 0$  m is recorded. All the velocity data are sampled at the cell centers. The sampling frequency is set to 1000 Hz, and the sampling duration is 30 s. The time step size  $\Delta t = 0.0005$  s is used in the simulations to ensure the Courant's number lower than 1. For each simulation case, the total simulation duration is 40 s, with the first 10 s of the simulation being excluded to eliminate any influence from the initial conditions.

### D. Experimental and simulation cases

For the sake of discussion in the following sections, all cases in this study are summarized in Table I. “SW” represents the flow produced by the static blade configuration, with the number at the end denoting the height of the maximum velocity at  $(x, y) = (3.0 \text{ m}, 0 \text{ m})$ . For example, “SW\_015” denotes the maximum velocity at  $z = 0.15$  m. The rotating blade configurations are described by the rotating angle of the blades in a specific order [Fig. 7(b)]. The clockwise rotating angle is stipulated to be the positive value. In addition, the prefix “NW” is used to denote the nonstationary wind flows produced by the rotating blade configuration. “NW\_015” and “NW\_025” are generated based on corresponding stationary winds with the maximum wind velocity at  $z = 0.15$  and  $0.25$  m. The rotating duration is combined by the values of  $\Delta t_1$ ,  $\Delta t_2$ , and  $\Delta t_3$  (Fig. 7). The wind velocity data in the present study can be obtained by point velocity measurements (PVM), PIV tests, and LES.

### III. NUMERICAL RESULTS VALIDATION

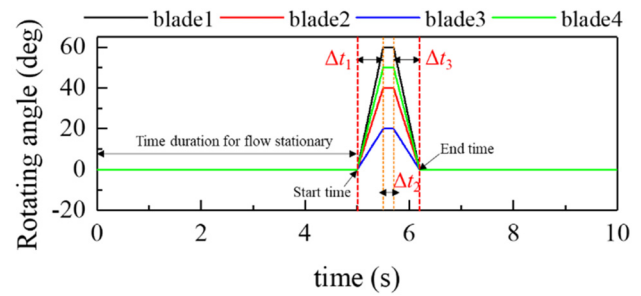
Before the simulation of the AMBS-generated flow fields, it is essential to validate the reasonability of the numerical results based on the wind tunnel tests. The wind profiles and nonstationary wind velocities of the ABMS-produced wind fields are compared with corresponding experimental results in Secs. III A and III B. In addition, the transient wind velocity patterns during the generation of nonstationary winds are also presented in Sec. III C for further comparison.

#### A. Wind profiles generated by static blade configuration

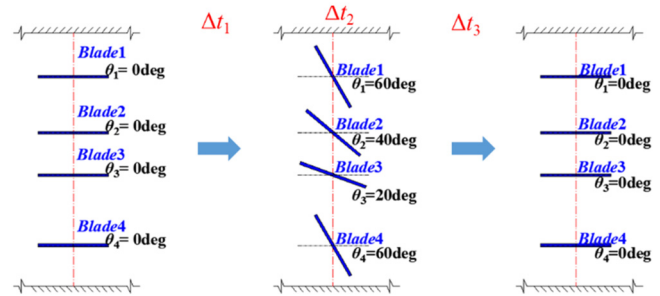
Vertical profiles of mean velocity and turbulence intensity at several locations ( $x = 1.5\text{--}4.5$  m) along the streamwise direction are

TABLE I. Wind field cases in the present study.

Cases	Rotating angle configurations	Rotating duration ( $\Delta t_1, \Delta t_2, \Delta t_3$ )	Methods
SW_015	$60^\circ - 40^\circ - 20^\circ - 60^\circ$	...	PVM & LES
SW_025	$35^\circ - 35^\circ - 35^\circ - 40^\circ$	...	PVM & LES
NW_015	$60^\circ - 40^\circ - 20^\circ - 60^\circ$	(0.5 s, 0.2 s, 0.5 s)	PVM & PIV & LES
NW_025	$35^\circ - 35^\circ - 35^\circ - 40^\circ$	(0.5 s, 0.2 s, 0.5 s)	PVM & PIV & LES



(a) Rotating angle time history



(b) Blade rotation schematic diagram

FIG. 7. Example of blade rotation time history and schematic diagram. (a) Rotating angle time history. (b) Blade rotation schematic diagram.

presented in Fig. 8. For validation purposes, the profiles acquired by wind tunnel measurements are also shown in the form of scattered points. Each velocity profile is normalized by the maximum wind velocity. The mean wind velocity profiles produced in the wind tunnel test were validated to be reasonable in our previous work (Yuan *et al.*, 2024) by comparing them with target full-scale downburst winds. It can be found that the wind profiles in the numerical simulation can match corresponding experimental measurements within an acceptable deviation. As shown in Fig. 8(a), the mean wind velocity profiles at  $x = 1.5\text{--}3.0$  m show a good agreement with the experimental results. However, as the flows further develop, the velocity profile in simulation tends to deviate from the corresponding experimental counterpart. In Fig. 8(b), only the turbulence intensity profiles below  $z = 0.6$  m are plotted. The experimentally measured turbulent velocity might deviate from the realistic value above  $z = 0.6$  m due to the effect of reversed flow in the upper region, which cannot be well measured by the Cobra Probe. It can be observed that the turbulence intensity below  $z = 0.3$  m is in good agreement with the experimental results. The

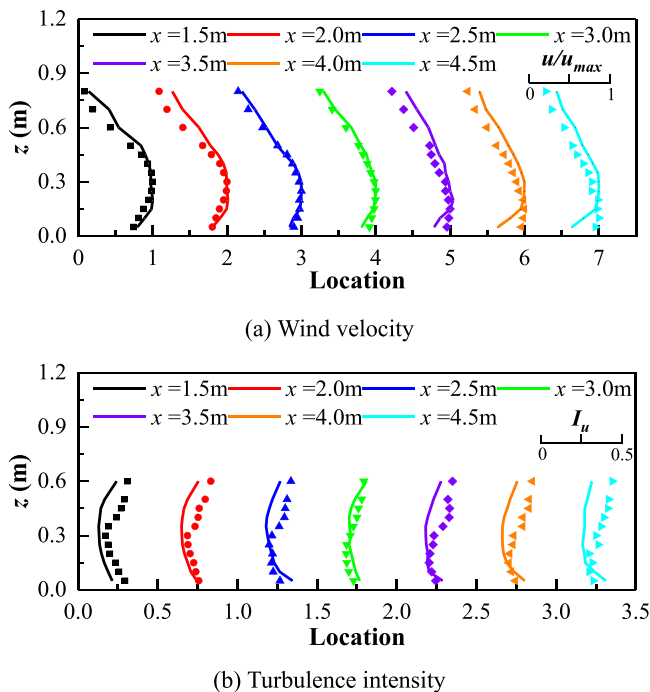


**FIG. 8.** Validation of wind profiles along the streamwise direction in SW\_025. (a) Wind velocity. (b) Turbulence intensity.

turbulence intensity profile around the horizontal location of  $x = 3.0$  m (turntable center of the wind tunnel) matches experimental measurements well.

### B. Nonstationary wind velocities produced by rotating blade configuration

To validate the nonstationary winds produced by the numerical simulation adopted in the present study, a nonstationary case is selected as a benchmark. The rotating blade configuration is set to be the same as that adopted in the wind tunnel test. Figure 9 shows the wind velocity time history obtained at the position of the maximum velocity at  $(x, y) = (3.0 \text{ m}, 0 \text{ m})$  during the blade rotation. The blade rotation starts at  $t = 10$  s. The velocity time history during  $t = 5$ – $15$  s is presented in this figure. It can be found that the numerical wind velocity time history is in good agreement with the experimental results,

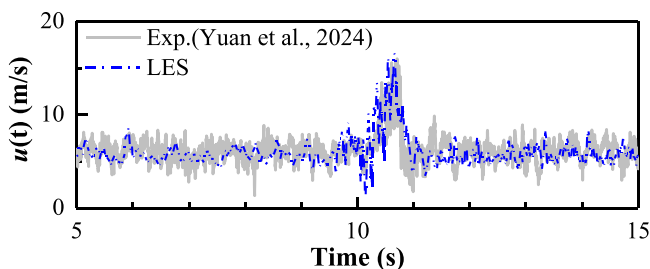


**FIG. 9.** Validation of nonstationary wind velocity at  $z = 0.15$  m in NW\_015.

although some deviation in fluctuation amplitude between them might still be observed. The ramp-up and ramp-down phenomenon of the wind velocity time history can be well simulated, and the peak velocity duration matches well with the experimental measurements.

### C. Transient wind velocity distribution

Furthermore, the spatial distribution of the velocity in LES is compared with that in the PIV test as the blades at their maximum rotation angle, i.e., at the stage of  $\Delta t_2$  shown in Fig. 7. For the ease of comparison, the time instant of the blades at the horizontal state is defined as zero. Two snapshots at  $t = 0.5$  and  $0.7$  s are shown in Figs. 10(a) and 10(b), respectively, which are captured in PIV measurements. At  $t = 0.5$  s, the rotating blades just reach their maximum rotation angle, and the blades keep their inclination state during  $t = 0.5$ – $0.7$  s. In addition, the velocity distribution at the same instants in LES is presented in Figs. 10(c) and 10(d). It should be noted that the velocity contours in LES are indicated in a reversed direction, while the coordinates for PIV and LES results are set according to the definition in Fig. 2. It can be observed that the primary vortex is produced almost at the same location ( $x = 3.0$  m) in PIV and LES at  $t = 0.5$  s. In addition, the other vortex can also be found with a relatively small size. The two vortices will further develop as time passes, which can be observed at  $t = 0.7$  s. The vortex height is increased with the development of flows. Therefore, the transient flow features can also be replicated in the LES, whereas the instantaneous velocity contour might have some discrepancies.

## IV. EVOLUTIONARY MECHANISMS OF AMBS-GENERATED FLOWS

Based on the validated numerical simulation method, the AMBS-generated winds are further investigated in terms of synchronous spatial features, which might be hard to capture through the wind tunnel test. The wind flows produced by static blade and rotating blade configurations are discussed in Secs. IV A and IV B, respectively.

### A. Stationary wind fields

The spatial features of AMBS-generated wind fields can be adjusted by the blade rotation configurations. In this section, the mean wind velocity distribution of the flows generated by static blade configuration is investigated as well as the vortex structures. Furthermore, the proper orthogonal decomposition (POD) analysis is conducted to identify spatiotemporal patterns in the AMBS-generated turbulent wind fields.

#### 1. Wind field structures

Figure 11 displays the mean wind velocity contours in three orthometric directions and the mean velocity vectors in SW\_025 and SW\_015. A notable increase in streamwise velocity downstream of the AMBS is evident in SW\_015, attributable to the augmented blade rotation angle directing more intense airflow downward. This results in the peak of the nose-shaped wind velocity profile appearing at a lower height. In addition, in SW\_015, the vertical velocity component is also increased, which manifests that the vertical velocity touching the ground can also be modified by appropriate adjustment of the blade rotation configuration. Therefore, the incidence angle of the downward flows can be controlled according to specific simulation objectives. As

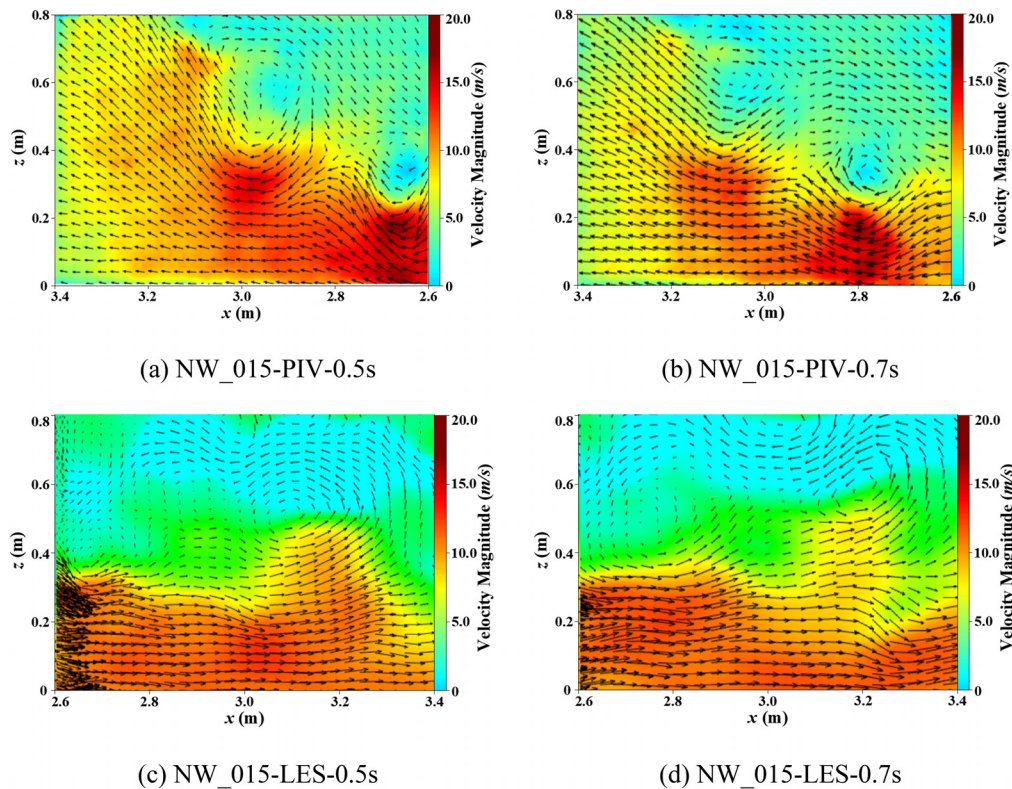


**FIG. 10.** Transient velocity contour and velocity vector as the flow impinging the ground. (a) NW\_015-PIV-0.5s; (b) NW\_015-PIV-0.7s; (c) NW\_015-LES-0.5s; and (d) NW\_015-LES-0.7s.

shown in Figs. 11(b) and 11(f), the spanwise velocity is negligible compared to the other components in the lower region. Conversely, in the upper region, the spanwise velocity is slightly increased. Additionally, the resultant mean wind velocity field is illustrated through velocity vectors in Figs. 11(d) and 11(h), representing the combined effect of streamwise and vertical velocity components. It can be observed that the mean velocity vectors tend to develop upward obliquely with the increase in streamwise distances.

Furthermore, to better understand the organized motions in the wind flows generated by the AMBS facility, the iso-surface of the  $Q$  value is utilized to investigate the development of vortex structures. Figure 12 depicts the vortex structures of the downburst-like outflows in SW\_025 and SW\_015. Notably, a series of columnar vortices can be observed in both cases, which are delineated with red lines in each sub-figure. For SW\_025, these columnar vortices tend to be dispersed with the flow evolving along the streamwise direction, in contrast to the phenomenon observed in SW\_015 where vortex movements present a more organized structure. Additionally, the vortex structures near the ground are also significantly affected by the rotation angle of the blades. Specifically, in SW\_015, elongated vortices are prominent near the wall, whereas in SW\_025, these vortices are noticeably smaller and less frequent. This variation could be attributed to the larger shear velocity of near-wall flows in SW\_015 compared to SW\_025, resulting in a significant stretching of the near-wall vortices due to enhanced kinetic energy.

## 2. POD analysis

To gain deeper insights into the structure of the flow field generated by the AMBS, the proper orthogonal decomposition (POD) approach is employed. This method, reviewed by Tamura *et al.* (1999), is effective for isolating deterministic structures that have physical significance. For this purpose, the wind velocity time history at the central plane, ranging from  $x = 1.5$  to  $4.0$  m, is extracted from the computational domain, as depicted in Fig. 13. The wind velocity data with a duration of 30 s are adopted for the POD analysis. In order to identify the most prominent energetic fluctuations in the AMBS-generated wind flows near the ground, the time-averaged velocity components are subtracted from the obtained numerical data. Thus, the residual fluctuating components of streamwise velocity, denoted as  $u(\mathbf{x}, t)$ , can be expressed as follows:

$$u(\mathbf{x}, t) = U(\mathbf{x}, t) - \bar{U}(\mathbf{x}, t) = \sum_{j=1}^n a_j(t) \phi_j(\mathbf{x}), \quad (2)$$

where  $\mathbf{x}$  denotes the spatial vector and  $\phi_i(\mathbf{x})$  and  $a_i(t)$  are the  $i$ -th spatial modes and corresponding time coefficients, respectively.

The core concept of the POD method is to find the deterministic coordinate system  $\phi_i$ , which has the optimal correlation with all the elements of a set of fluctuating velocity fields. To determine the modal features and corresponding energy contribution by different

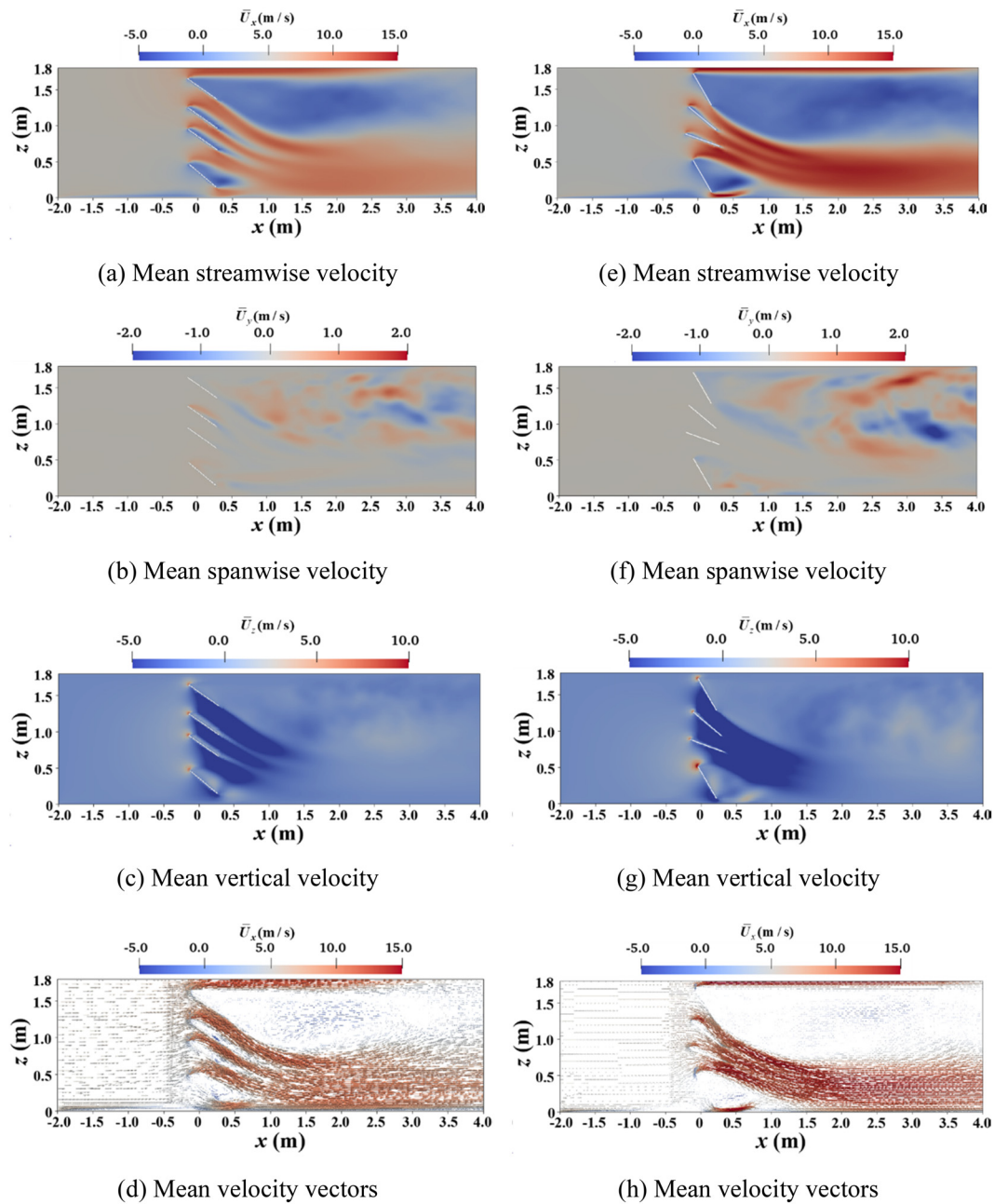


**FIG. 11.** Wind velocity contours and vectors in SW\_025 (a)–(d) and SW\_015 (e)–(h). (a) and (e) Mean streamwise velocity; (b) and (f) mean spanwise velocity; (c) and (g) mean vertical velocity; and (d) and (h) mean velocity vectors.

modes, the most direct method is to solve the eigenvalue problem as follows:

$$\hat{R}_v \phi = \lambda \phi, \quad (3)$$

where  $\hat{R}_v = \overline{u(x_i, y_i, t)u(x_j, y_j, t)}$  is the space covariance,  $\phi$  is the eigenvector matrix, and  $\lambda$  is the corresponding eigenvalue vector.

The fluctuating velocity field can be reconstructed by the following equation:

$$u(x, y, t) = \sum_{m=1}^M \delta_m(t) \phi_m(x, y), \quad (4)$$

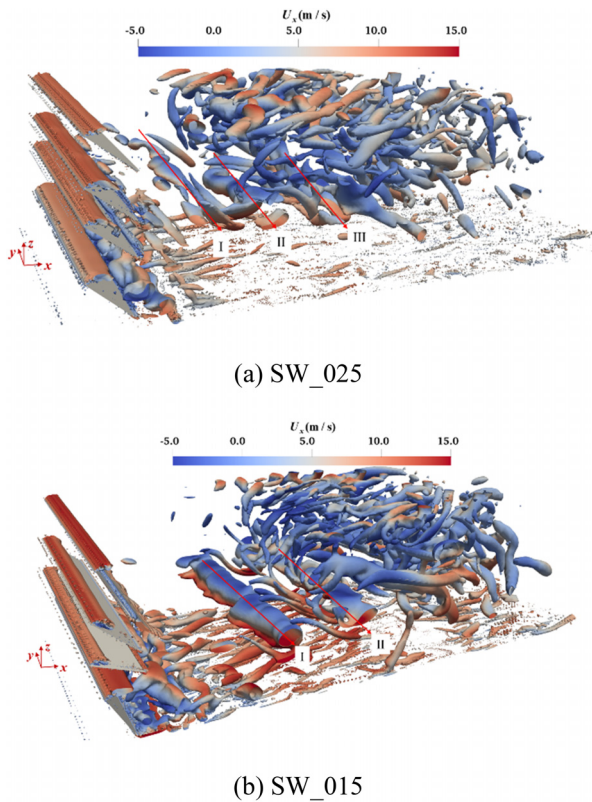


FIG. 12. The iso-surface of  $Q=1200$  is colored by streamwise velocity. (a) SW\_025 and (b) SW\_015.

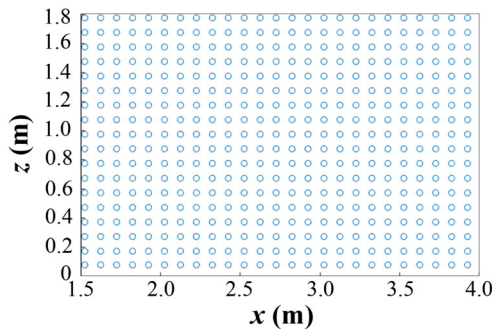


FIG. 13. Monitoring points arrangement at the central vertical plane ( $y=0$  m).

where  $\delta_m$  is the principal coordinate, which denotes the expansion coefficient of each mode.

Figure 14 shows the energy distribution of the first 20 POD modes of the flow field in SW\_025. The energy contribution of each mode is described by the proportion of corresponding eigenvalues in all POD modes. As plotted in Fig. 14, the cumulative energy contribution of modes 1–20 takes over 70% of the total energy, which implies that a small number of POD modes might be capable of describing the primary features of the flow field. The energy contributions of Modes

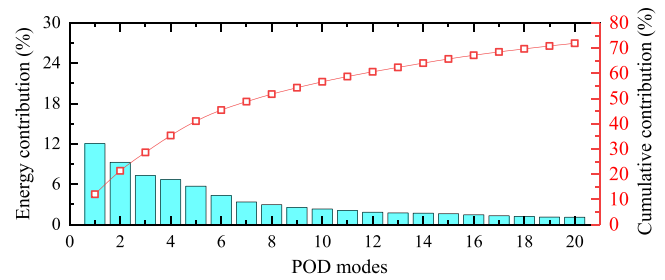


FIG. 14. Cumulative energy of POD modes and energy distribution of modes 1–20.

1–6 are, respectively, 12.1%, 10.3%, 8.3%, 7.7%, 6.7%, and 6.3%, with a sum of over 50% of the total energy. The contributions of other higher modes are all decreased to smaller than 5%, which means a limited effect on the whole flow field. To this end, only the first six modes are selected for the following analysis.

Figure 15 elucidates the contour patterns and spectral characteristics of the principal coordinates for Modes 1–6 of the AMBS-generated flow in SW\_025. The energy contributions of each mode are annotated in the titles of the corresponding subfigures. In addition, the normalized spectrum of the principal coordinate  $\delta_m$  for each mode is defined as  $S_\delta / (S_\delta)_{\max}$ , expressed as a function of the reduced frequency  $fz_{\max} / u_{\max}$ . As shown in Fig. 15(a), Mode 1 presents in-phase fluctuations across all locations, with the lower altitude region characterized by two distinct areas of opposing modal phases. The negative region, appearing at around  $x=3.0$  m, is much larger than the positive one and reaches down to the near-ground region. This negative region means that the local velocity is lower than the mean velocity in the corresponding mode, which might be attributed to the primary vortex produced in the adjacency region. The main frequency of the principal coordinate of Mode 1 is about  $fz_{\max} / u_{\max} = 0.03$ , representing the prevalent frequency within this flow regime. For Mode 2, the modal pattern is dominated by a positive region, exhibiting a main frequency roughly double that of Mode 1. As depicted in Fig. 15(c), the pattern of Mode 3 is constituted by three regions where the signs of their modal phases vary alternately. It can be observed that the negative and positive regions at  $x=3.7$  extend to the ground. Modes 3–6, characterized by their multiple frequency components, demonstrate that vortices are dominated by varied frequencies and scales, leading to intricate modal patterns [as shown in Figs. 15(d)–15(f)]. Consequently, the airflow dynamics within the primary vortex zone are modulated by multiple modes with disparate frequencies, which contribute to the complexity of the vortices observed in Fig. 11(a).

## B. Nonstationary wind fields

The nonstationary wind fields can be produced by the rotating blades with specific configurations. However, in the wind tunnel test, one can only obtain the nonstationary features of the generated wind field from PVM at a few locations. The evolutionary features of the wind field during the generation of nonstationary winds might be hard to obtain. To this end, the characteristics of nonstationary wind fields during the blade rotation are investigated based on the LES considering its superiority in extracting full-field information quantitatively. First, the transient wind velocity profile during the generation of a

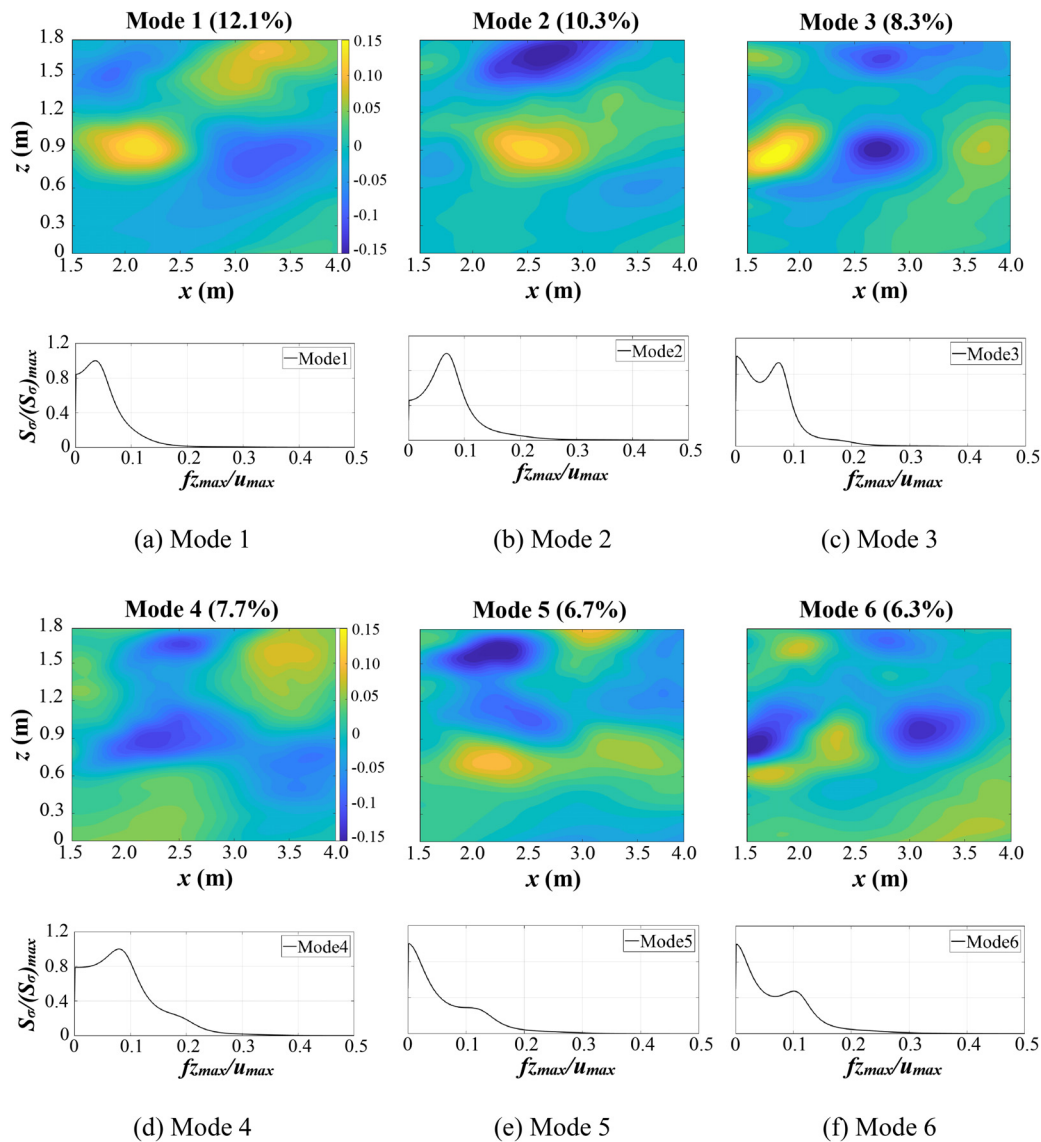


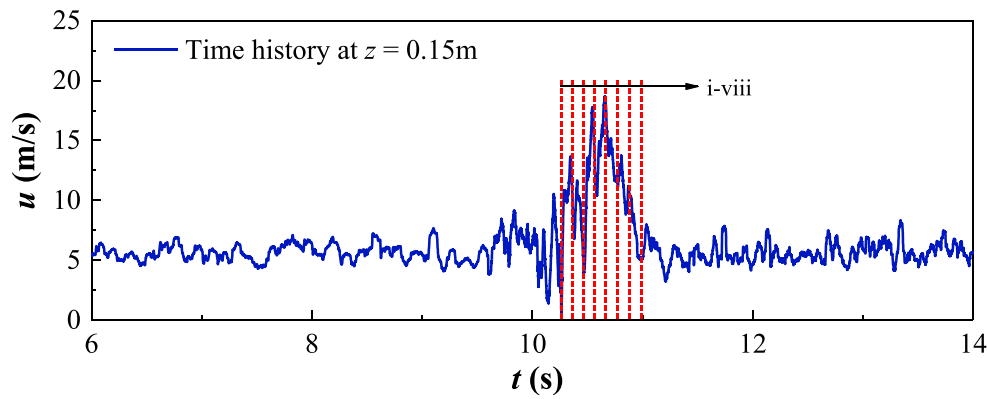
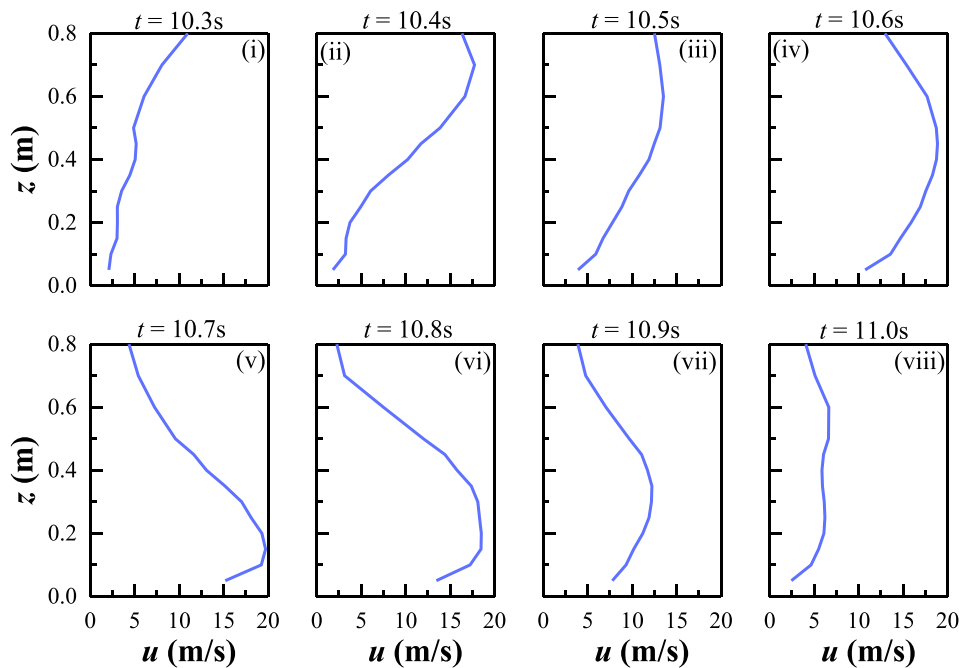
**FIG. 15.** Contours and the spectra of the principal coordinates of POD modes 1–6 for flows in SW\_025: (a) Mode 1; (b) Mode 2; (c) Mode 3; (d) Mode 4; (e) Mode 5; and (f) Mode 6.

nonstationary wind field is analyzed. Additionally, the variations of wind velocity patterns are also investigated.

### 1. Evolutionary features of wind profiles

Figure 16 presents the evolution of the vertical wind velocity profiles at the turntable center (i.e.,  $x = 3.0$  m). We extracted and displayed wind velocity profiles at eight distinct moments, ranging from 10.3 to 11.0 s, in Fig. 16(b). The wind velocity time history plotted in Fig. 16(a) is monitored at  $z = 0.15$  m. The instants are also marked by dashed lines with the designation of i–viii. As depicted in Fig. 16(a), at  $t = 10.7$  s, the ramp-up interval of the nonstationary winds is completed, and the maximum value of  $u$  is achieved. At this

time, the typical nose-shaped downburst profile is well developed with the maximum velocity occurring at  $z = 0.15$  m, as shown in Fig. 16(b). The evolutionary process of the velocity profile closely resembles full-scale downburst events recorded at the Port of Livorno on 13 September 2015 (Burlando *et al.*, 2017; Solari *et al.*, 2020). It should be mentioned that, after  $t$  exceeds 10.7 s, the nose-shape profile is further developed, while the maximum velocity is decreased, and its corresponding height is increased [Fig. 15(b)(vi–vii)]. At  $t = 11.0$  s, the wind velocity profile becomes uniform, signaling the end of the ramp-down phase of the nonstationary wind velocity time history. In contrast, during the ramp-up stage, an inverse trend can be observed that the height of the maximum velocity decreases over time, as shown in Fig. 16(b)(i–iv).

(a) Time history of  $u$ (b) Vertical profiles of  $u$  at different instances

**FIG. 16.** Variation of vertical wind velocity profiles during the generation of nonstationary winds. (a) Time history of  $u$ . (b) Vertical profiles of  $u$  at different instances.

## 2. Evolutionary features of vortex structures

To elucidate the flow variation during the generation of nonstationary wind fields, several specific instants are adopted for detailed discussion. Figure 17 shows the contours of the streamwise and vertical velocity components. Before the blade rotation ( $t = 10$  s), the streamwise velocity distributes uniformly, with the vertical velocity nearly negligible. When each blade rotates to a specific angle, as depicted in Figs. 17(b) and 17(g), both the streamwise and vertical velocities are significantly increased in the lower region. In the cases of  $t = 10.7$  s

and 10.75 s, all the blades reach their maximum rotation angle for this numerical case. It is observed that the region of maximum streamwise velocity near the ground shifts from  $x = 2.0$  m to 3.0 m. Furthermore, at  $t = 10.75$  s, the vertical velocity at  $x = 2.5$ –3.5 m is significantly increased compared with that at  $t = 10.7$  s, which implies the enhancement of upward flows. At  $t = 10.9$  s, the blades are during the stage of reverting to their original state, which results in an apparent decrease in the maximum velocity and the increase in its corresponding height.

Figure 18 presents the velocity vectors corresponding to the five instants discussed in Fig. 17. The arrows in each subfigure are

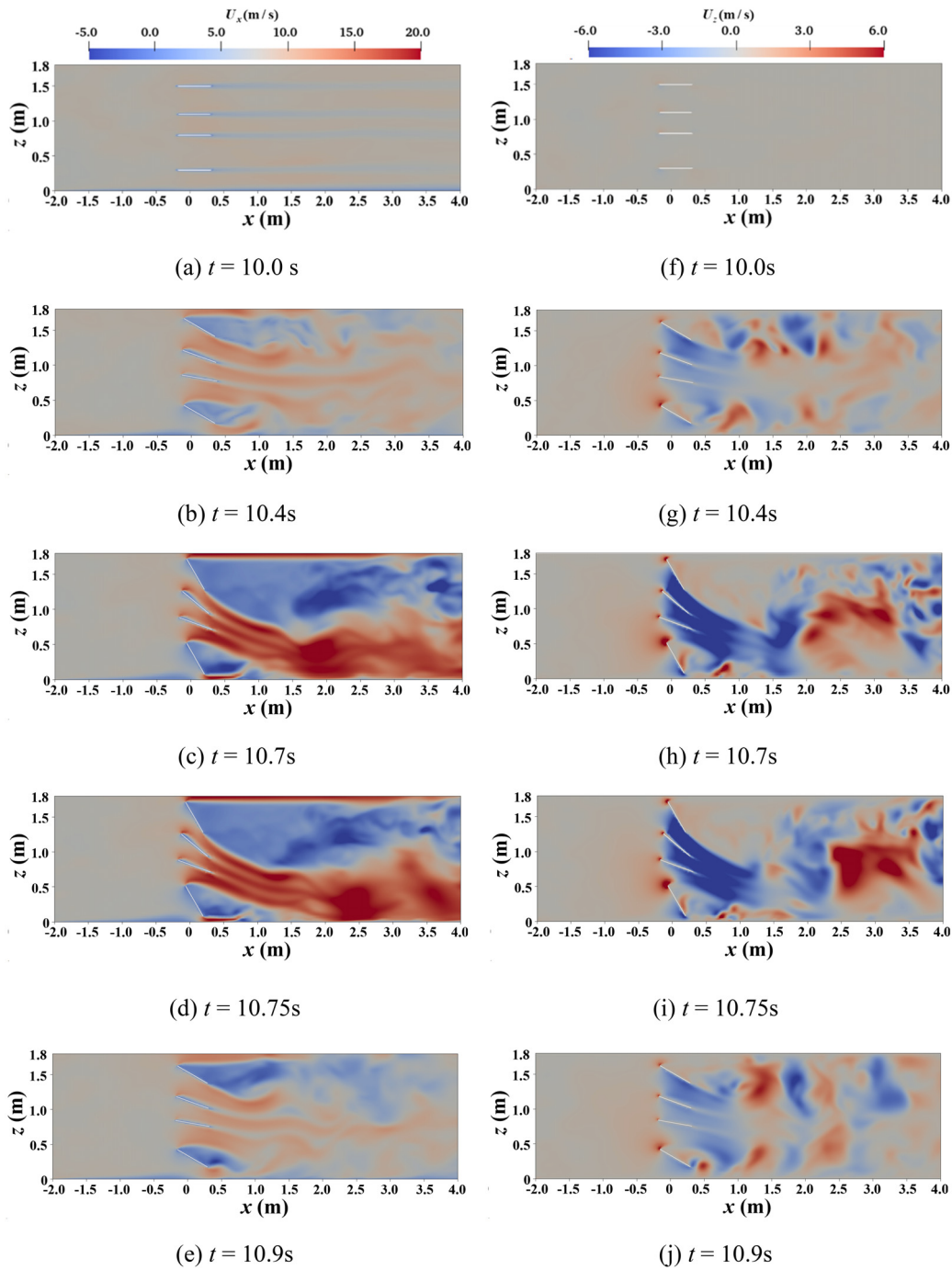


**FIG. 17.** The streamwise (a)–(e) and vertical velocity (f)–(j) contours during the blade rotation. (a) and (f)  $t = 10.0$  s; (b) and (g)  $t = 10.4$  s; (c) and (h)  $t = 10.7$  s; (d) and (i)  $t = 10.75$  s; (e) and (j)  $t = 10.9$  s.

scaled and colored according to the streamwise velocity. Figures 18(c) and 18(d) demonstrate the presence of a primary vortex, with its migration from  $x = 2.0$  to  $2.5$  m. However, at  $t = 10.75$  s, the primary vortex tends to dissipate due to the increase in

upward vertical wind velocity. Before and after the blades reach their maximum rotation angle, such as at  $t = 10.4$  and  $10.9$  s, no obvious rolling vortex formation is observed in the lower height region.

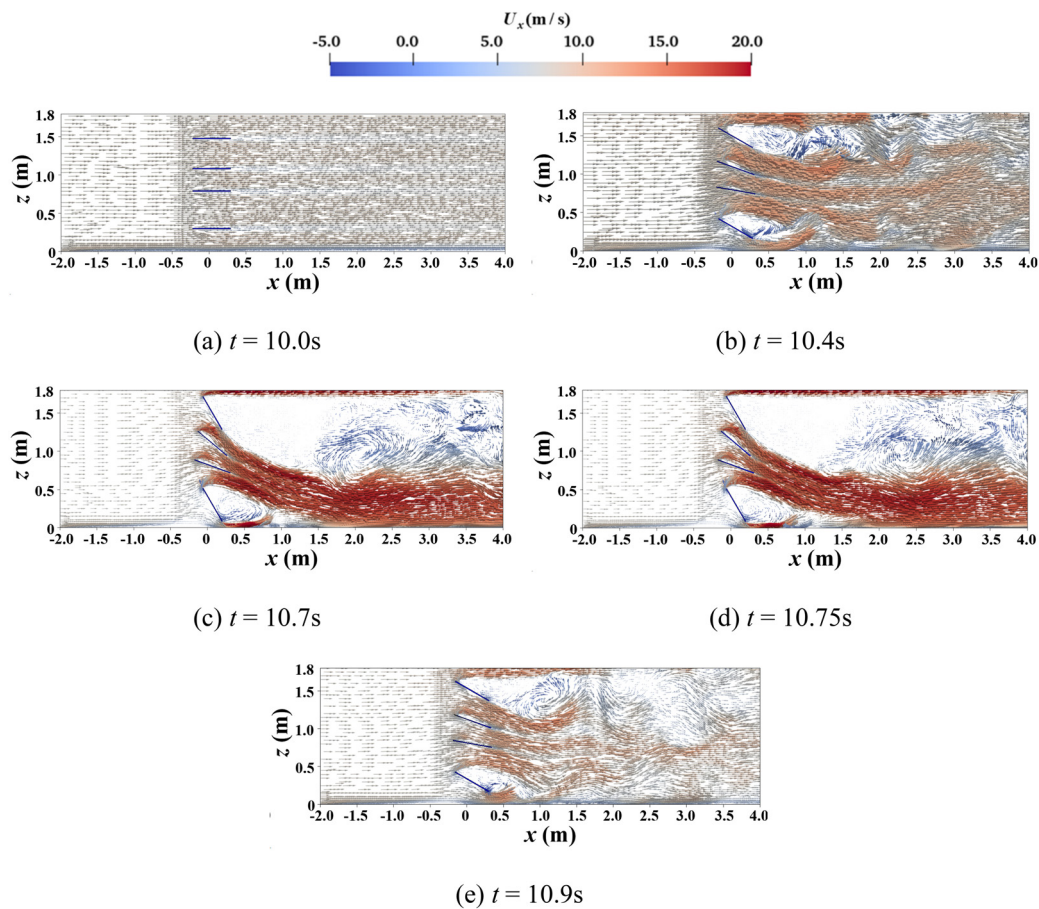


**FIG. 18.** The velocity vectors colored by streamwise velocity. (a)  $t = 10.0$  s; (b)  $t = 10.4$  s; (c)  $t = 10.7$  s; (d)  $t = 10.75$  s; and (e)  $t = 10.9$  s.

## V. CONCLUDING REMARKS

This paper deepens the understanding of downburst-like winds generated by the AMBS, utilizing both large-eddy simulation (LES) and Particle Image Velocimetry (PIV) measurements. First, the wind profiles and nonstationary wind velocities obtained by LES are validated by the point velocity measurements using the AMBS facility. This includes a comparative analysis of the mean wind velocity profiles, distribution patterns of velocity vectors, and wind velocity time history with corresponding experimental results. Furthermore, the present study explored the spatial characteristics of wind flows induced by static blade configurations through detailed flow structure investigation and proper orthogonal decomposition (POD) analysis. The wind field evolution features during the generation of nonstationary downburst-like outflows are also elucidated from the aspect of the spatial distribution of wind velocity. The main findings from the present study are summarized as follows:

(1) The LES method effectively replicates the vertical mean wind velocity profiles along the streamwise direction, although minor discrepancies emerge with the flow development. The time history of nonstationary wind velocity in the numerical simulation

aligns closely with experimental measurements. Furthermore, it is proved that the LES method can well simulate the evolution of the primary vortex observed in the PIV test during the flow impinging on the ground.

- (2) The mean wind field pattern can be adjusted customizably by the blade angle combinations in static blade configurations. A series of columnar vortexes are produced in the case of static blade configuration, with apparently organized structures being produced as the maximum velocity is concentrated at a lower height.
- (3) For the flows generated by the static blade configuration, the cumulative energy contributions of the first three modes constitute more than half of the total energy within the fluctuating wind field. The vortex at the horizontal position from  $x = 2.5$  to  $3.0$  m is shaped by a convergence of multiple flow modes, each distinguished by its unique frequency.
- (4) The typical nose-shaped profile can be well developed at the target region during the generation of nonstationary winds. During the velocity ramp-up phase, the height of maximum velocity decreases over time, and the nose-shaped wind velocity profile is gradually formed at the turntable center. Conversely,

in the ramp-down phase, the height of maximum velocity is increased with decreasing wind speed, eventually leading to a more uniform profile.

- (5) For nonstationary winds generated by rotating blade configurations, the primary vortex is formed as the downward flow impinges on the ground. This vortex tends to dissipate over time, even while the blades maintain their maximum rotation angle. The ramp-up and ramp-down of the generated nonstationary wind velocity are mainly attributed to the two phenomena.

## ACKNOWLEDGMENTS

The authors would like to acknowledge the financial support from the National Natural Science Foundation of China (Nos. 52221002 and 52278483), the 111 Project of China (No. B18062), the Natural Science Foundation of Chongqing, China (No. cstc2022ycjh-bgzxm0050), the S&T Program of Hebei (No. 225676162GH), and the Fundamental Research Funds for the Central Universities (Nos. 2023CDJXY-030 and 2024CDJZCQ-011).

## AUTHOR DECLARATIONS

### Conflict of Interest

The authors have no conflicts to disclose.

## Author Contributions

**Yangjin Yuan:** Conceptualization (equal); Data curation (equal); Formal analysis (equal); Investigation (equal); Methodology (equal); Software (equal); Validation (equal); Visualization (equal); Writing – original draft (equal). **Bowen Yan:** Conceptualization (equal); Funding acquisition (equal); Project administration (equal); Supervision (equal); Writing – review & editing (equal). **Xuhong Zhou:** Supervision (equal). **Xiao Li:** Conceptualization (equal); Resources (equal); Writing – review & editing (lead). **You Dong:** Conceptualization (equal); Supervision (equal); Writing – review & editing (equal). **Qingshan Yang:** Funding acquisition (equal); Project administration (equal); Supervision (equal). **Qingquan Liu:** Funding acquisition (equal).

## DATA AVAILABILITY

The data that support the findings of this study are available from the corresponding author upon reasonable request.

## REFERENCES

- Abd-Elaal, E.-S., Mills, J. E., and Ma, X., “An analytical model for simulating steady state flows of downburst,” *J. Wind Eng. Ind. Aerodyn.* **115**, 53–64 (2013).
- Aboshosha, H., Bitsuamlak, G., and El Damatty, A., “Turbulence characterization of downbursts using LES,” *J. Wind Eng. Ind. Aerodyn.* **136**, 44–61 (2015).
- Aboutabikh, M., Ghazal, T., Chen, J., Elgamal, S., and Aboshosha, H., “Designing a blade-system to generate downburst outflows at boundary layer wind tunnel,” *J. Wind Eng. Ind. Aerodyn.* **186**, 169–191 (2019).
- Asano, K., Iida, Y., and Uematsu, Y., “Laboratory study of wind loads on a low-rise building in a downburst using a moving pulsed jet simulator and their comparison with other types of simulators,” *J. Wind Eng. Ind. Aerodyn.* **184**, 313–320 (2019).
- Butler, K. and Kareem, A., “Physical and numerical modeling of downburst generated gust fronts,” in *Proceedings of the 12th International Conference on Wind Engineering* (IEEE, Cairns, Australia, 2007).
- Butler, K. and Kareem, A., “Characteristics of surface pressures on prismatic models in simulated gust front outflows,” in *The Seventh Asia-Pacific Conference on Wind Engineering* (APCWE7, Taipei, Taiwan, 2009).
- Burlando, M., De Cio, A., Pizzo, M., and Solari, G., “Analysis of wind vertical profiles of thunderstorm events in the Mediterranean,” in *Proceedings of 9th Asia-Pacific Conference On Wind Engineering* (APCWE9, Auckland, New Zealand, 2017).
- Canepa, F., Burlando, M., and Solari, G., “Vertical profile characteristics of thunderstorm outflows,” *J. Wind Eng. Ind. Aerodyn.* **206**, 104332 (2020).
- Fujita, T., *The Downburst-Micoburst and Macrobust Report of Projects NIMROD and JAWS* (The University of Chicago, 1985).
- Fang, Z., Wang, Z., Li, Z., Yan, J., and Huang, H., “Wind field characteristics of stationary and moving downbursts based on the test of impinging jet with a movable nozzle,” *J. Wind Eng. Ind. Aerodyn.* **232**, 105266 (2023).
- Hjelmfelt, M. R., “Structure and life cycle of microburst outflows observed in Colorado,” *J. Appl. Meteorol. Climatol.* **27**(8), 900–927 (1988).
- Hangan, H., Refan, M., Jubayer, C., Parvu, D., and Kilpatrick, R., “Big data from big experiments. The WindEEE dome,” in *Whither Turbulence and Big Data in the 21st Century?*, edited by A. Pollard, L. Castillo, L. Danaila, and M. Glauser (Springer International Publishing, 2017a), pp. 215–230.
- Hangan, H., Refan, M., Jubayer, C., Romanic, D., Parvu, D., LoTufo, J., and Costache, A., “Novel techniques in wind engineering,” *J. Wind Eng. Ind. Aerodyn.* **171**, 12–33 (2017b).
- Hangan, H., Romanic, D., and Jubayer, C., “Three-dimensional, non-stationary and non-Gaussian (3D-NS-NG) wind fields and their implications to wind-structure interaction problems,” *J. Fluid Struct.* **91**, 102583 (2019).
- Ibrahim, I., Aboshosha, H., and El Damatty, A., “Numerical characterization of downburst wind field at WindEEE dome,” *Wind Struct.* **30**(3), 231–243 (2020).
- Jesson, M., Sterling, M., Letchford, C. W., and Baker, C., “Aerodynamic forces on the roofs of low-, mid- and high-rise buildings subject to transient winds,” *J. Wind Eng. Ind. Aerodyn.* **143**, 42–49 (2015a).
- Jesson, M., Sterling, M., Letchford, C. W., and Haines, M., “Aerodynamic forces on generic buildings subject to transient, downburst-type winds,” *J. Wind Eng. Ind. Aerodyn.* **137**, 58–68 (2015b).
- Junayed, C., Jubayer, C., Parvu, D., Romanic, D., and Hangan, H., “Flow field dynamics of large-scale experimentally produced downburst flows,” *J. Wind Eng. Ind. Aerodyn.* **188**, 61–79 (2019).
- Kim, J. and Hangan, H., “Numerical simulations of impinging jets with application to downbursts,” *J. Wind Eng. Ind. Aerodyn.* **95**(4), 279–298 (2007).
- Kwon, D. K. and Kareem, A., “Gust-front factor: New framework for wind load effects on structures,” *J. Struct. Eng.* **135**(6), 717–732 (2009).
- Kwon, D. K. and Kareem, A., “Towards codification of thunderstorm/downburst using gust front factor: Model-based and data-driven perspectives,” *Eng. Struct.* **199**, 109608 (2019).
- Liu, M., Pan, Y., Hu, J., Zhang, C., Yu, X., and Xie, Z., “A field measurement study of intense thunderstorm outflows characteristics based on a 356 m high meteorological tower,” *J. Wind Eng. Ind. Aerodyn.* **242**, 105590 (2023).
- Li, C., Li, Q. S., Xiao, Y. Q., and Ou, J. P., “A revised empirical model and CFD simulations for 3D axisymmetric steady-state flows of downbursts and impinging jets,” *J. Wind Eng. Ind. Aerodyn.* **102**, 48–60 (2012).
- Le, T. H. and Caracoglia, L., “Computer-based model for the transient dynamics of a tall building during digitally simulated Andrews AFB thunderstorm,” *Comput. Struct.* **193**, 44–72 (2017).
- Le, V. and Caracoglia, L., “Generation and characterization of a nonstationary flow field in a small-scale wind tunnel using a multi-blade flow device,” *J. Wind Eng. Ind. Aerodyn.* **186**, 1–16 (2019).
- Mason, M. S., Letchford, C. W., and James, D. L., “Pulsed wall jet simulation of a stationary thunderstorm downburst, Part A: Physical structure and flow field characterization,” *J. Wind Eng. Ind. Aerodyn.* **93**(7), 557–580 (2005).
- Mason, M. S., Wood, G. S., and Fletcher, D. F., “Numerical simulation of downburst winds,” *J. Wind Eng. Ind. Aerodyn.* **97**(11–12), 523–539 (2009).
- Mejia, A. D., Elawady, A., Vutukuru, K. S., Chen, D., and Chowdhury, A. G., “Examination of different wall jet and impinging jet concepts to produce large-scale downburst outflow,” *Front. Built Environ.* **8**, 980617 (2022).

- Romanic, D., LoTufo, J., and Hangan, H., "Transient behavior in impinging jets in crossflow with application to downburst flows," *J. Wind Eng. Ind. Aerodyn.* **184**, 209–227 (2019).
- Sengupta, A. and Sarkar, P. P., "Experimental measurement and numerical simulation of an impinging jet with application to thunderstorm microburst winds," *J. Wind Eng. Ind. Aerodyn.* **96**(3), 345–365 (2008).
- Solari, G., "Thunderstorm response spectrum technique: Theory and applications," *Eng. Struct.* **108**, 28–46 (2016).
- Solari, G., Burlando, M., and Repetto, M. P., "Detection, simulation, modelling and loading of thunderstorm outflows to design wind-safer and cost-efficient structures," *J. Wind Eng. Ind. Aerodyn.* **200**, 104142 (2020).
- Tamura, Y., Suganuma, S., Kikuchi, H., and Hibi, K., "Proper orthogonal decomposition of random wind pressure field," *J. Fluid Struct.* **13**(7–8), 1069–1095 (1999).
- Wood, G. S., Kwok, K. C., Motteram, N. A., and Fletcher, D. F., "Physical and numerical modelling of thunderstorm downbursts," *J. Wind Eng. Ind. Aerodyn.* **89**, 535–552 (2001).
- Wu, Z., Iida, Y., and Uematsu, Y., "The flow fields generated by stationary and traveling downbursts and resultant wind load effects on transmission line structural system," *J. Wind Eng. Ind. Aerodyn.* **210**, 104521 (2021).
- Yan, B. W., Yuan, Y. J., Ma, C. Y., Dong, Z. C., Huang, H. J., and Wang, Z. S., "Modeling of downburst outflows and wind pressures on a high-rise building under different terrain conditions," *J. Build. Eng.* **48**, 103738 (2022).
- Yuan, Y. J., YAN, B. W., Zhou, X. H., Li, X., Yang, Q. S., Zhou, X., and Shu, Z. R., "An active-controlled multi-blade facility to generate 2-D downburst-like outflows in the boundary layer wind tunnel," *J. Wind Eng. Ind. Aerodyn.* **248**, 105713 (2024).
- Zhang, H., Wang, H., Xu, Z., Zhang, Y., Tao, T., and Mao, J., "Monitoring-based analysis of wind-induced vibrations of ultra-long stay cables during an exceptional wind event," *J. Wind Eng. Ind. Aerodyn.* **221**, 104883 (2022).
- Zhang, Y., Sarkar, P., and Hu, H., "An experimental study on wind loads acting on a high-rise building model induced by microburst-like winds," *J. Fluids Struct.* **50**, 547–564 (2014).
- Zhang, S., Yang, Q., Solari, G., Li, B., and Huang, G., "Characteristics of thunderstorm outflows in Beijing urban area," *J. Wind Eng. Ind. Aerodyn.* **195**, 104011 (2019).
- Zuzul, J., Ricci, A., Burlando, M., Blocken, B., and Solari, G., "CFD analysis of the WindEEE dome produced downburst-like winds," *J. Wind Eng. Ind. Aerodyn.* **232**, 105268 (2023).